MRS Advances
https://doi.org/10.1557/s43580-025-01355-z

ORIGINAL PAPER

Understanding spin waves in 2D magnets: A combined experimental, computational, and mathematical theory approach

Piper J. Aislinn[1] · Anthony J. Winchell[1] · Evan R. Lambertson[2] · Patrick Moret[2] · Tim J. Zuehlsdorff[2] · Nikolaus Elsaesser[3] · Johannes A. Huurman[3] · Axel I. Saenz Rodriguez[3] · Zdenek Sofer[4] · Pallavi Dhagat[5] · Oksana Ostroverkhova[1]

Received: 28 March 2025 / Accepted: 24 July 2025

Abstract

We present our work towards developing a comprehensive approach to understanding spin-wave (SW) dispersion in 2D van der Waals (vdW) magnets, combining steady-state and time-resolved spectroscopy with electronic structure calculations and mathematical modeling of SW propagation. Exploiting magnon–exciton coupling in CrSBr, we utilize time-resolved reflectance to detect a novel regime of optically generated resonances at 77 and 87 GHz and investigate their origin with magnetic field dependence. We use density functional theory (DFT) calculations of magnetic exchange couplings to model the impact of strain on coupling parameters in CrSBr and present a theoretical framework to determine dispersion characteristics based on quantum field theory (QFT), an alternate to the Landau–Lifshitz equation (LL) approach predominantly used in the literature. Our combined approach allows for the incorporation of additional parameters that more accurately describe the properties of the material into SW models.

Introduction

Artificial intelligence and cryptocurrency have intensified the environmental costs of computing due to power-intensive cooling to dissipate resistive heating. Spintronics offers a low-power alternative for high-performance computing by replacing electrons with magnons—quanta of spin waves—which enable energy-efficient information processing, nanoscale wave-based computing [1], communications, and quantum sensing [2]. Unlike electrons, magnons possess no resistive heating [2]. However, understanding how material properties and external conditions control spin-wave velocity, anisotropy, and coherence lengths is crucial for applications in signal processing and communications.

Two-dimensional (2D) materials provide a promising platform for spintronics due to their highly tunable properties [3]. Recent demonstrations of spin-wave generation, magnon–exciton coupling, strong exciton–photon coupling (polariton formation), and magnetotransport in 2D magnetic materials have laid the foundations for systematic studies of magnons and their interactions in novel quantum magnets [2, 4–10].

The benchmark 2D magnet CrSBr, a direct bandgap 2D van der Waals (vdW) semiconductor with easy-plane antiferromagnetic order (Fig. 1a), and Néel temperature of about 130 K and 150 K for bulk and monolayer samples, respectively, [11] exhibits exciton–magnon coupling, which enables generating, characterizing, and controlling spin-wave propagation via optical methods [5–7]. Laser pulse-generated magnons with frequencies in the tens of GHz range and group velocities on the order of km/s, depending on beam parameters, magnetic field, and sample thickness, have been demonstrated using time-resolved reflectance [6, 7, 12]. However, the mechanisms and dominant interactions that govern magnon dispersion remain debated [6, 12, 13].

This paper discusses a comprehensive approach towards understanding spin-wave propagation in 2D magnets,

✉ Oksana Ostroverkhova
oksana@science.oregonstate.edu

[1] Department of Physics, Oregon State University, Corvallis 97331, OR, USA

[2] Department of Chemistry, Oregon State University, Corvallis 97331, OR, USA

[3] Department of Mathematics, Oregon State University, Corvallis 97331, OR, USA

[4] Department of Inorganic Chemistry, University of Chemistry and Technology Prague, Prague 6 166 28, Czech Republic

[5] Department of Electrical Engineering and Computer Science, Oregon State University, Corvallis 97331, OR, USA

Published online: 06 August 2025

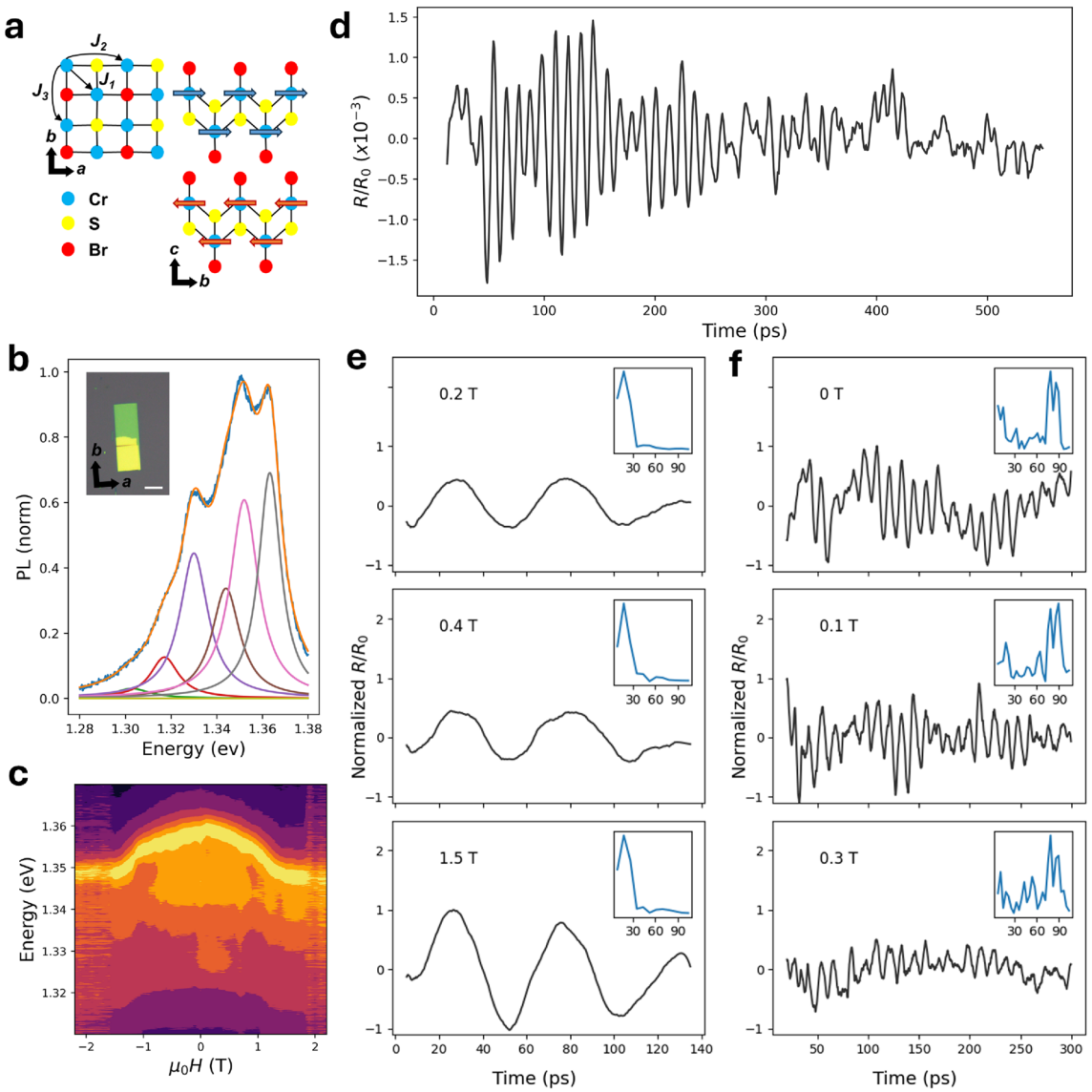

Fig. 1 **a** CrSBr forms in rectangular sheets (a-b plane) that stack via vdW bonds along the c-axis. Layers are ferromagnetic (magnetic easy axis along b), but couple antiferromagnetically to adjacent layers. **b** PL from 10-nm flake at 1.6 K. Fits with Lorentzian peak functions are included to analyze the emission structure. Inset shows an image of the flake (blue region is 10 nm and yellow region is 24 nm thick). Scale bar is 10 μm. **c** PL vs. magnetic field (applied in the out-of-plane direction, along the c-axis). Exciton energies show a quadratic decrease with increasing field up to the saturation field. **d** TRR in the 10-nm flake exhibiting beats, **e-f** B-dependent TRR in the 364-nm and 10-nm flakes, respectively, normalized to the maximum amplitude in respective samples. Fourier transforms of the data are included as insets, x-axis is frequency in GHz)

integrating experiments with density functional theory (DFT) calculations, classical Landau–Lifshitz (LL) theory, and quantum field theory (QFT). In CrSBr, we observe thickness-dependent optically generated resonances at 22 GHz, 77 GHz, and 87 GHz, with different magnetic field dependencies. While the 22 GHz resonance due to coherent magnon generation was previously observed in CrSBr flakes, [6, 12, 14] the high-frequency resonances have not yet been demonstrated or predicted theoretically. We compare LL and QFT models to derive magnon dispersion relations and spin correlations depending on various parameters such as DFT-calculated exchange coupling constants. While phenomenological LL theory underpins current micromagnetic simulations, its limitations highlight the need for alternative approaches such as QFT, which accounts for quantum spin effects and explicitly incorporates material parameters (e.g., lattice constants and symmetry). This integration advances the design of materials with tailored dispersion relations optimized for particular applications.

Methods

Materials and sample preparation

CrSBr forms rectangular sheets that bond along the c-axis via vdW interactions (Fig. 1a). Within layers, CrSBr is ferromagnetic (FM) with spins aligned along the b-axis; interlayer coupling is antiferromagnetic (AFM).

Bulk CrSBr crystals were prepared by chemical vapor transport of elements in a quartz ampule. Samples were mechanically exfoliated from bulk crystals, deposited on SiO_2/Si, and characterized by atomic force and optical microscopy.

Measurements

The samples were placed in an optical cryomagnet (Quantum Design OptiCool). Photoluminescence was measured under 532 nm optical excitation of a flake through a 20x objective (0.4 NA) with sub-micron resolution at 1.6-300 K and at 0-3 T magnetic field applied out-of-plane (along the c-axis). For time-resolved reflectance (TRR) microscopy, 10 kHz laser pulses were generated using the 1030 nm fundamental output of a pulsed laser (Light Conversion Pharos) that seeded a 50-fs 532 nm pump pulse (average power of 10-20 μW) and a 910 nm probe pulse (Light Conversion Orpheus-N and -F), which were focused through a 20x objective to a ~20 micron-sized spot, with pump-probe time delays in the 0-950 ps range. This yielded a pump pulse energy of 1-2 nJ and an instantaneous peak power of 20-40 kW. The TRR data were collected at various out-of-plane magnetic fields at 1.6 K on two flakes that were 10-nm and 364-nm thick.

Density-functional theory (DFT) calculations

To obtain theoretical predictions for magnetic exchange parameters in CrSBr, density functional theory (DFT) calculations on CrSBr monolayer were performed using the CASTEP electronic structure package [15] as detailed in the Supporting Information. Additionally, the sensitivity of magnetic couplings with respect to externally applied strain and finite-temperature effects due to the experimentally predicted thermal expansion of the material were investigated.

Results

Experiment: optically induced resonances

At 1.6 K, PL emission exhibits dominant exciton emission in the ~1.35−1.37 eV region near the A-exciton (Fig. 1b) [16]. A magnetic field applied out-of-plane shifts the PL emission to lower energies (Fig. 1c), due to exciton delocalization across layers enabled by spin alignment with the field, until the saturation field of ~2 T is reached [5, 8, 16–18].

The absorption of a 532 nm pump pulse induces a change in the equilibrium spin configuration, and the resulting spin precession is detected as a change in reflectivity near the A-exciton resonance (Fig. 1d-f). Oscillations are observed, persisting up to at least 300 ps after excitation. In the thicker flake, a fast-Fourier transform reveals a dominant magnon mode at 22 GHz, consistent with the generation of coherent magnons described in the literature [6, 12]. The amplitude of the oscillations for the 364-nm flake increased with the magnetic field up to about 1.5 T, followed by about a 20% decrease at 2 T (Fig. 1e), also consistent with the literature. [16] Interestingly, in the thin 10-nm flake, large oscillations with dominant frequencies of 77 GHz and 87 GHz were observed at zero field, with amplitudes decreasing with increasing field (Fig. 1f). These frequencies are considerably higher than the two modes previously observed under optical excitation in CrSBr (about 24 and 33 GHz) [6, 7, 12]. A distinct beating pattern was also observed (Fig. 1d).

The observation of such varied resonant behavior and the quest to understand its origin motivate an exploration of the parameters influencing magnon dispersion. Development of a complete understanding is beyond the scope of this article, and it requires systematic evaluation of how magnon properties can be tuned by parameters accessible via sample geometry, experimental conditions, and material design. However, as a first step towards this goal, we examine one such variable—internal and induced strain. Using DFT, we explore how strain influences exchange coupling and, consequently, magnon dispersion.

DFT calculations: effect of strain on exchange parameters

The isotropic exchange coupling parameters J_1, J_2, and J_3 (see Fig. 1a) are defined by the spin Hamiltonian

$$\mathcal{H} = \sum_{\langle ij \rangle} J_{ij} \mathbf{S}_i \cdot \mathbf{S}_j. \tag{1}$$

To determine these parameters as a function of crystal strain ϵ_a and ϵ_b, we compare the difference in DFT+U energies from four different spin-orderings referred to as FM, AFM_1,

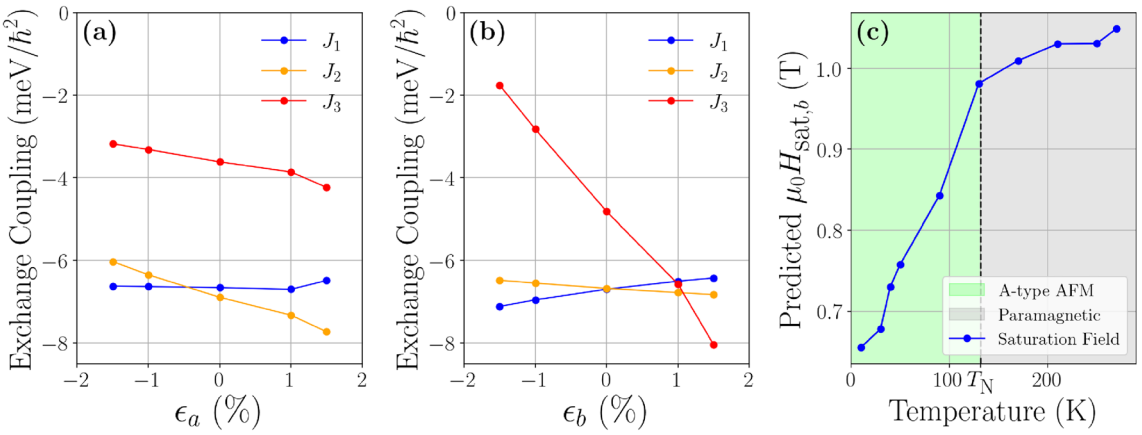

Fig. 2 Intralayer exchange couplings as a function of **a** *a*- and **b** *b*-axis strain computed from monolayer CrSBr. **c** Predicted *b*-axis saturation field as a function of temperature, considering only the effect of thermal lattice expansion on the exchange parameters

AFM_2, and AFM_3 (see SI Fig. 2) in monolayer CrSBr cells. These orderings are used to extract the individual exchange parameters from the total energy, the details of which are outlined in the SI. Here, the strain percentage is defined as the proportional change of the unit cell parameters relative to the optimized ground-state FM geometry. For each ϵ, the corresponding lattice vector is fixed across the four different magnetic orderings within each layer, while the orthogonal in-plane lattice vector and atomic positions are allowed to relax. The resulting energies then determine J_1, J_2, and J_3 according to Eq. 1 of the SI.

Panels (a) and (b) of Fig. 2 show how the intralayer couplings evolve with strain applied along the *a*- and *b*-axes of monolayer CrSBr. The three nearest-neighbor intralayer exchange parameters are consistent with experimental [13] and theoretical [19, 20] values previously obtained. Within the experimentally accessible range (up to $\pm 1.5\%$) [7], all three couplings J_1, J_2, and J_3 do not change significantly with respect to strain along the *a*-axis. For $\pm 1.5\%$ strain along the *a*-axis, the couplings are $J_1 \approx -6.6$ meV/$\hbar^2$, $J_2 \approx -6.0$ meV/$\hbar^2$, and $J_3 \approx -3.2$ meV/$\hbar^2$ at -1.5% strain, while at $+1.5\%$ strain they are $J_1 \approx -6.5$ meV/$\hbar^2$, $J_2 \approx -7.7$ meV/$\hbar^2$, and $J_3 \approx -4.2$ meV/$\hbar^2$. However, the parameter J_2, which directly couples spins along this axis, exhibits the greatest variation. Likewise, J_3 varies appreciably with strain along the *b*-axis, differing by nearly a factor of four between the fully compressed and stretched limits. For $\pm 1.5\%$ strain along the *b*-axis, the couplings are $J_1 \approx -7.1$ meV/$\hbar^2$, $J_2 \approx -6.5$ meV/$\hbar^2$, and $J_3 \approx -1.8$ meV/$\hbar^2$ at -1.5% strain, and $J_1 \approx -6.4$ meV/$\hbar^2$, $J_2 \approx -6.8$ meV/$\hbar^2$, and $J_3 \approx -8.0$ meV/$\hbar^2$ at $+1.5\%$ strain.

DFT calculations: mean-field estimate of the saturation field

A mean-field estimate (see Sec. 1.3 of the SI) of the *b*-axis saturation field computed from lattice parameters measured at various temperatures in bulk CrSBr is shown in Fig. 2c [21]. Here, the *b*-axis saturation field refers to the field required to disrupt the interlayer AFM ordering and saturate spin alignment along *b*. We emphasize that temperature is only implicitly accounted for via the lattice configurations, and that all other explicit effects are neglected. As a result, the transition of the saturation field to 0 T at the Néel temperature $T_N = 132\ K$ is inherently missing. The predicted saturation field appears to exhibit two temperature-dependent regimes separated at T_N and each increasing with temperature. This observation is consistent with previous findings that isotropic exchange interactions drive lattice relaxation in CrSBr [22]. Moreover, the increase indicates that thermally induced lattice relaxation competes with the spin disorder caused by thermal fluctuations and thereby contributes to a larger Néel temperature than would otherwise be observed [23–26]. Lastly, we note that previously reported *b*-axis saturation fields at temperatures approaching 0 K are slightly lower than the values predicted here (approximately 0.37−0.5 T) [23–26].

Theoretical modeling

We develop computations to analyze the dispersion relation of layered 2D spin systems through *quantum field theory (QFT)*

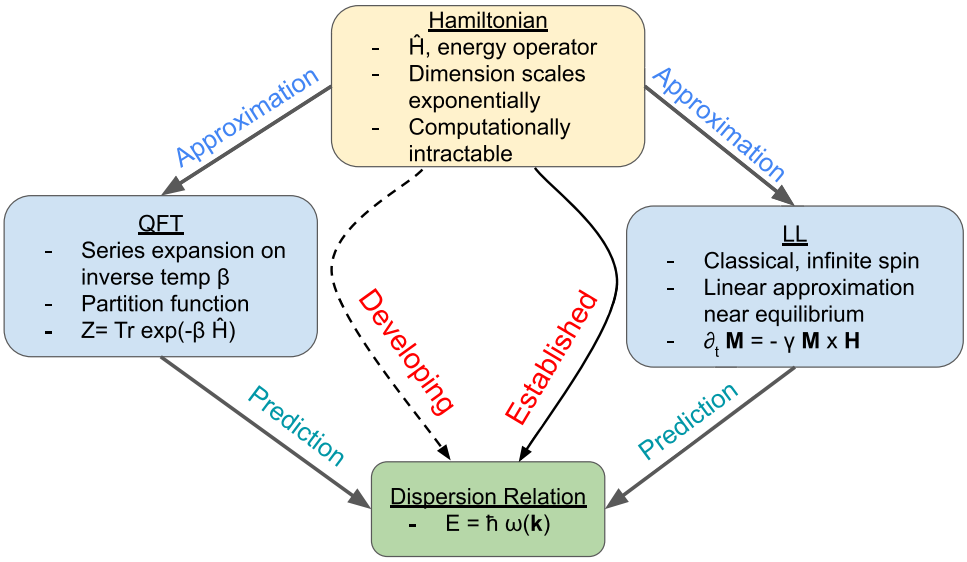

Fig. 3 We develop a novel approach to obtain dispersion relations for 2D layered magnets via QFT computations. The established approach is based on the Landau–Lifshitz equation, e.g., [6, 12]. We aim to understand the compatibility of both approaches

path integral series expansion as an alternative to the approach via *Landau–Lifshitz (LL) equations* in the literature. Numerical computations for quantum systems are challenging since the dimension of the system grows exponentially with the system size. We develop QFT computations as a robust numerical technique to introduce a variety of external forces and couplings through first principles to investigate non-linear effects, inherently absent in linearized approximations such as the LL equations (Fig. 3).

QFT computations are well suited for analyzing many different materials and the effect of external forces such as magnetic field—many of the model parameters may be included in the computations—but there is a trade-off between accuracy and computational power. The input for QFT computations is as follows: (1) a discrete lattice Λ, (2) an external magnetic field $\vec{H}(v) = (H_+(v), H_-(v), H_z(v))$ for $v \in \Lambda$, and (3) an interaction tensor $V_{i,j}(v, w)$ for $i, j = +, -, z$ and $v, w \in \Lambda$. The input for our QFT computation corresponds to the following Hamiltonian for a spin system with quadratic interactions

$$\mathcal{H} = -\left(\frac{g\mu_\beta}{\hbar} \sum_{v\in\Lambda} \vec{H}(v) \cdot \vec{S}(v) + \sum_{\substack{v,w\in\Lambda \\ i,j\in\{+,-,z\}}} V_{i,j}(v,w) S_i(v) S_j(w) \right), \tag{2}$$

where $S_i(v)$ is the i-spin operator, $i = -, +, z$, at vertex $v \in \Lambda$. In our computations, we consider the following Hamiltonian

$$\mathcal{H} = -\frac{g\mu_\beta}{2\hbar} \sum_{v\in\Lambda} \vec{H}(v) \cdot \vec{S}(v) - \frac{1}{2} \sum_{v,w\in\Lambda} J(v,w) \left(\vec{S}(v) \cdot \vec{S}(w) \right) - \frac{g^2 \mu_\beta^2 \mu_0}{2\hbar^2} \sum_{v,w\in\Lambda} \left(\frac{\vec{S}(v) \cdot \vec{S}(w)}{|v-w|^3} - 3 \frac{[\vec{S}(v) \cdot (v-w)][\vec{S}(w) \cdot (v-w)]}{|v-w|^5} \right), \tag{3}$$

where μ_β is the Bohr magneton, g is the Landé factor, and μ_0 is the vacuum magnetic permeability. The first, second, and third terms correspond to the energy from the external magnetic field, the energy from the spin–spin interactions, and the energy from the dipole interactions, respectively, see [27, Ch. 2 Sec. 7] for a derivation of this Hamiltonian. A strength of the QFT approach is that we may introduce other external forces or couplings by adding corresponding terms to the Hamiltonian.

Detailed description of the QFT computations has been given for a general spin chain system [28] and a square-lattice, layered 2D spin system with spin–spin exchange and dipole interactions [29]. The latter work discusses the limitations of the LL approach and the discrepancies between the LL and QFT approaches specifically for 2D systems. The direct application of the typical differential LL equations fails, and instead QFT recovers (pseudodifferential) LL equations for thin films when taking a perturbative limit near the equilibrium point. In the case of the square lattice, the dispersion relation for a bilayer system with external magnetic field perpendicular to the plane for two spin-wave modes is given by [29]

$$\omega_1(\vec{k}) = \left(\Omega(\vec{k})\left(\Omega(\vec{k}) + \frac{2\pi\mu_0 g^2\mu_\beta^2 B(p)k}{\hbar^2 a^2}(1+e^{-kd})\right)\right)^{1/2}$$
$$\omega_2(\vec{k}) = \left(\left(\Omega(\vec{k}) + 2B(p)J'\right)\left(\Omega(\vec{k}) + 2B(p)J' + \frac{2\pi\mu_0 g^2\mu_\beta^2 B(p)k}{\hbar^2 a^2}(1-e^{-kd})\right)\right)^{1/2}, \quad (4)$$

where a and d are lattice parameters defined in Fig. 4a, $\vec{k} = (k_x, k_y)$ is the wave number with $k = |\vec{k}|$, $B(p_0)$ is the average S_z-magnetization for a spin with external magnetic field $\vec{H} = (0, 0, H)$ and no other interactions so that $p_0 = H\beta g\mu_\beta$ and $\beta = 1/(k_B T)$ (i.e., the inverse of the Boltzmann constant times temperature),

$$\Omega(\vec{k}) = \frac{g\mu_\beta}{\hbar}(H + H_{dm}) + 2B(p)J(2 - \cos(k_x a) - \cos(k_y a)) \quad (5)$$

is the frequency from the effective magnetic field and the spin–spin exchange within the same layer, $p = \beta g\mu_\beta|\vec{H} + \vec{H}_s|$, $H = |\vec{H}|$ is the strength of the external magnetic field, $H_{dm} = |\vec{H}_{dm}|$ is the strength of the demagnetization field arising from the dipole interactions, and $H_s = |\vec{H}_s|$ is the strength of the field induced from the spin–spin exchange—derivation of the induced and demagnetization fields is given in the SI. The dispersion relation of Eq.(4) differs from the dispersion relation given in [12] obtained from LL equations (Fig. 4), which is most evident in the explicit dependence of the thickness of the lattice d that is missing in [12]. This demonstrates that the QFT has the potential to capture qualitative features of the layered systems, through first principles, that are absent via a phenomenological application of the LL equations.

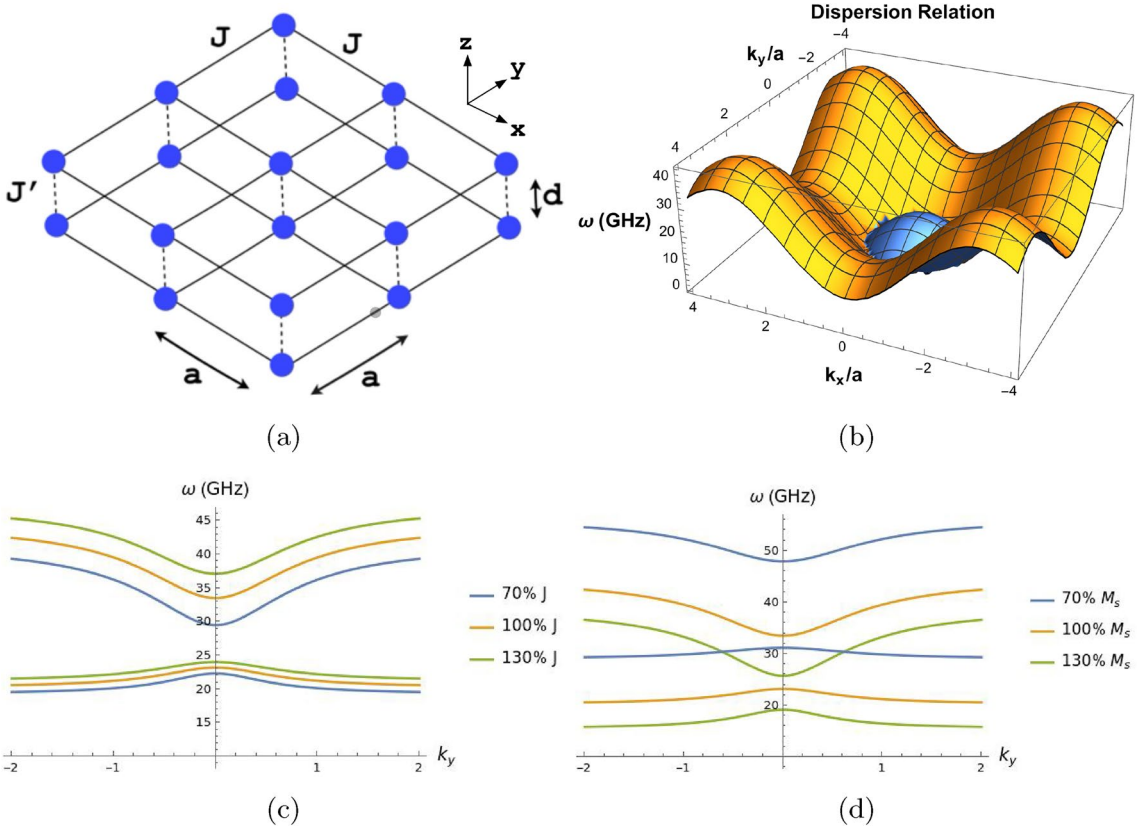

Fig. 4 Dispersion relations via Landau–Lifshitz equations and QFT computations. **a** For QFT, we take a spin-1/2 system with spin–spin exchange and dipole interactions on a 3x3x2 cubic lattice, with exchange energies $(J, J') = (-3.38\ \text{meV}/\hbar^2, 0.05\ \text{meV}/\hbar^2)$, lattice spacing (a, d) = (3.508 Å, 7.959 Å) labeled, and an external magnetic field $H = 0.01$ T perpendicular to the plane. **b** The dispersion curve obtained from QFT computations of Eq.(4) for temperature $T = 6$ K. There are two modes plotted with similar frequencies. At zero wave numbers, the frequency of the two modes is $\omega_1 = 11.20$ GHz and $\omega_2 = 11.41$ GHz. **c**-**d** For LL, we recreate the computations in [12] and consider the effect of the spin-exchange coupling (**c**) and the effect of the magnetic saturation (**d**)

We consider the effect of external forces on spin-wave propagation through the dispersion relations obtained by the LL equations [12]; see (c) and (d) in Fig. 4. We input different values of spin–spin exchange coupling constants guided by results in the DFT computations in Fig. 2a-b. The QFT computations presented here are a test case on a system with similar features as CrSBr, and we obtain frequencies in the right order of magnitude compared to the LL computations in Fig. 4c-d and [12]. They serve as a base point for further development of our novel QFT approach, which will more accurately resemble the experimental conditions under different external forces and couplings.

Our current QFT computations need to be adapted as follows to accurately account for the experimental conditions: (1) use spin-3/2 operators instead of spin-1/2 operators, (2) include anisotropy terms in the Hamiltonian (Fig. 1a), (3) include additional external forces and couplings in the Hamiltonian, (4) add more layers to the system, (5) increase the dimensions of each layer, (6) change the geometry of the lattice to a hexagonal lattice, and (7) compute higher order terms in the series expansion.

Discussion

Coherent magnons launched with the laser pulses have previously been demonstrated in CrSBr using both TRR and time-resolved MOKE [6, 12, 14, 16]. Launching mechanisms based on the laser-induced demagnetization field and transient strain fields due to strong magnetoelastic coupling were proposed to describe the acoustic (33 GHz, due to shear stress) and optical (24 GHz, due to pressure stress) magnon modes [14].

The coherence length and group velocity of optically excited magnons in CrSBr vary with thickness; [12] however, the previously reported shift in magnon frequencies was only ~10% from bilayer to bulk [6]. The 77 and 87 GHz resonances observed in our 10-nm flake (Fig. 1f), but not in our 364-nm flake (Fig. 1e), which have high amplitude at zero field that decreases with increasing field, have not been previously reported. Given the recent observations of fluence-dependent magnon-mediated non-linear excitonic interactions in CrSBr observed via intensity-dependent exciton energy shifts, [16] we hypothesize that the higher pump pulse energy combined with a shorter pulse duration used in our experiments (resulting in a three orders of magnitude higher instantaneous peak power than that in previous work [6]) enable excitation of high-frequency acoustic and magnetoacoustic resonances via strong magnon–phonon coupling. For example, in magnetic $[Co/Pd]_n$ multilayers in Ref. [30], the ultrafast laser induced an acoustic wave, which via a strong magnon–phonon coupling led to a magnetoacoustic resonance with a 60 GHz frequency for n = 11 (film thickness of 25 nm), explained in a framework of the strain–spin interactions. Spin–phonon coupling in CrSBr has been previously observed via temperature-dependent Raman signatures, [31] but further work is needed to establish the exact mechanisms, conditions for the observation, and the applications of high-frequency resonances in Fig. 1f.

The beating patterns in TRR signals from CrSBr (e.g., similar to those in Fig. 1d) have previously been attributed to the non-linear magnon dispersion due to the high spectral content of the wave packet generated by a focused pump beam, which resulted in a distribution of the magnon density of states that manifests as beats in the envelope of the spin-wave packet [12]. However, beats in TRR can be present due to acoustic contributions as well, [32] and so the origin of the beats in Fig. 1d needs further clarification.

The magnon dispersion calculated using the LL approach in CrSBr accounting for interlayer coupling, triaxial anisotropy, and dipolar interactions [33] revealed contributions of various interactions in the magnon properties. For example, inclusion of the dipolar interaction increased the magnon frequency by 11% (near the Γ-point) in the monolayer and bilayer CrSBr. The high-frequency resonances (77 GHz and 87 GHz) observed in our experiments (Fig. 1d and 1f) are not predicted by the LL approach with reasonable offsets (e.g., differences in the inherent strain or magnetization saturation [34]) in parameters used to accurately describe the 24 and 33 GHz modes (Fig. 4c-d) [6, 12]. The QFT approach expanded the range of possible input parameters which expanded the range of predicted magnon frequencies. However, more work is needed to understand the most critical parameters and underlying mechanisms that determine the magnon dispersion characteristics and to incorporate the effects of strain–spin interactions.

Conclusion

We observed optically induced resonances in CrSBr with drastically different frequencies and behavior under applied magnetic fields, depending on the sample thickness, and developed theoretical and computational approaches to incorporate more material- and sample geometry-specific parameters. We will continue developing these approaches which will be applied to understanding properties of magnetic materials and developing design principles for novel magnets with magnon properties optimized for specific applications.

Supplementary Information The online version contains supplementary material available at https://doi.org/10.1557/s43580-025-01355-z.

Acknowledgments We thank J. Chan and C. Cleveland for assistance with sample preparation and Dr. S. Ahmed for assistance with time-resolved reflectance calibration.

Author Contributions Z. S. synthesized bulk crystals; P. A. and A. W. prepared samples and collected data; E. L., P. M., and T. J. Z. performed DFT calculations; N. E., J. H., and A. S. R. developed theoretical models and simulated spin dynamics; and O. O. and P. D. supervised the project. All authors wrote and edited the manuscript.

Funding This work was supported by the Oregon State University College of Science SciRis program and the Simons Foundation via Pivot Fellowship (to A. S. R. and O. O.).

Sample fabrication and characterization were performed in a user facility enabled by the National Science Foundation DMR-1920368 grant.

Z. S. was supported by project LUAUS25268 from Ministry of Education Youth and Sports (MEYS) and by the project Advanced Functional Nanorobots (reg. No. CZ.02.1.01/0.0/0.0/15_003/0000444 financed by the ERDF).

Data Availability Data sets generated during the current study are available from the corresponding author on reasonable request.

Declarations

Conflict of interest The authors declare no Conflict of interest.

References

1. G. Csaba, Á. Papp, W. Porod, Phys. Lett. A **381**, 1471–1476 (2017)
2. B. Flebus et al., J. Phys.: Condens. Matter **36**, 363501 (2024)
3. M. Zeng, Y. Xiao, J. Liu, K. Yang, L. Fu, Chem. Rev. **118**, 6236–6296 (2018)
4. X. Jiang, Q. Liu, J. Xing, N. Liu, Y. Guo, Z. Liu, J. Zhao, Appl. Phys. Rev. **8**, 031305 (2021)
5. M.E. Ziebel, M.L. Feuer, J. Cox, X. Zhu, C.R. Dean, X. Roy, Nano Lett. **24**, 4319–4329 (2024)
6. Y.J. Bae, J. Wang, A. Scheie, J. Xu, D.G. Chica, G.M. Diederich, J. Cenker, M.E. Ziebel, Y. Bai, H. Ren, C.R. Dean, M. Delor, X. Xu, X. Roy, A.D. Kent, X. Zhu, Nature **609**, 282–286 (2022)
7. G.M. Diederich, J. Cenker, Y. Ren, J. Fonseca, D.G. Chica, Y.J. Bae, X. Zhu, X. Roy, T. Cao, D. Xiao, X. Xu, Nat. Nanotechnol. **18**, 23–28 (2023)
8. F. Dirnberger, J. Quan, R. Bushati, G.M. Diederich, M. Florian, J. Klein, K. Mosina, Z. Sofer, X. Xu, A. Kamra, F.J. Garca-Vidal, A. Alú, V.M. Menon, Nature **620**, 533–537 (2023)
9. T. Wang, D. Zhang, S. Yang, Z. Lin, Q. Chen, J. Yang, Q. Gong, Z. Chen, Y. Ye, W. Liu, Nat. Commun. **14**, (2023)
10. E.J. Telford, A.H. Dismukes, K. Lee, M. Cheng, A. Wieteska, A.K. Bartholomew, Y.-S. Chen, X. Xu, A.N. Pasupathy, X. Zhu, C.R. Dean, X. Roy, Adv. Mater. **32**, 2003240 (2020)
11. K. Lee, A.H. Dismukes, E.J. Telford, R.A. Wiscons, J. Wang, X. Xu, C. Nuckolls, C.R. Dean, X. Roy, X. Zhu, Nano Lett. **21**, 3511–3517 (2021)
12. Y. Sun, F. Meng, C. Lee, A. Soll, H. Zhang, R. Ramesh, J. Yao, Z. Sofer, J. Orenstein, Nat. Phys. **20**, 794–800 (2024)
13. A. Scheie, M. Ziebel, D.G. Chica, Y.J. Bae, X. Wang, A.I. Kolesnikov, X. Zhu, X. Roy, Adv. Sci. **9**, 2202467 (2022)
14. Y.J. Bae, T. Handa, Y. Dai, J. Wang, H. Liu, A. Scheie, D.G. Chica, M.E. Ziebel, A.D. Kent et al., Phys. Rev. B **109**, (2024)
15. S.J. Clark, M.D. Segall, C.J. Pickard, P.J. Hasnip, M.I.J. Probert, K. Refson, M.C. Payne, Zeitschrift f ur Kristallographie **220**, (2005)
16. B. Datta, P.C. Adak, S. Yu, A.V. Dharmapalan, S.J. Hall, A. Vakulenko, F. Komissarenko, E. Kurganov, J. Quan, W. Wang et al., Nat. Mater. **24**, 1027 (2025)
17. J. Cenker, S. Sivakumar, K. Xie, A. Miller, P. Thijssen, Z. Liu, A. Dismukes, J. Fonseca, E. Anderson, X. Zhu, X. Roy, D. Xiao, J.-H. Chu, T. Cao, X. Xu, Nat. Nanotechnol. **17**, 256–261 (2022)
18. N.P. Wilson, K. Lee, J. Cenker, K. Xie, A.H. Dismukes, E.J. Telford, J. Fonseca, S. Sivakumar, C. Dean, T. Cao, X. Roy, X. Xu, X. Zhu, Nat. Mater. **20**, 1657–1662 (2021)
19. D. L. Esteras, A. Rybakov, A. M. Ruiz, J. J. Baldov , Nano Letters 22, Published online September 26, 2022; in issue November 2022, 8771-8778 (2022)
20. Y. Wang, N. Luo, J. Zeng, L.-M. Tang, K.-Q. Chen, Phys. Rev. B **108**, 054401 (2023)
21. S.A. López-Paz, Z. Guguchia, V.Y. Pomjakushin, C. Witteveen, A. Cervellino, H. Luetkens, N. Casati, A.F. Morpurgo, F.O. von Rohr, Nat. Commun. **13**, 4745 (2022)
22. C. Boix-Constant, S. Mañas-Valero, A.M. Ruiz, A. Rybakov, K.A. Konieczny, S. Pillet, J.J. Baldov, E. Coronado, Adv. Mater. **34**, 2204940 (2022)
23. C. Ye, C. Wang, Q. Wu, S. Liu, J. Zhou, G. Wang, A. Söll, Z. Sofer, M. Yue, X. Liu, M. Tian, Q. Xiong, W. Ji, X. Renshaw Wang, ACS Nano **16**, 11876–11883 (2022)
24. F. Long, K. Mosina, R. Hübner, Z. Sofer, J. Klein, S. Prucnal, M. Helm, F. Dirnberger, S. Zhou, Appl. Phys. Lett. **123**, 222401 (2023)
25. M.E. Ziebel, M.L. Feuer, J. Cox, X. Zhu, C.R. Dean, X. Roy, Nano Lett. **24**, 4319–4329 (2024)
26. L. Krelle, R. Tan, D. Markina, P. Mondal, K. Mosina, K. Hagmann, R. von Klitzing, K. Watanabe, T. Taniguchi, Z. Sofer, B. Urbaszek, Magnetic correlation spectroscopy in crsbr, arXiv:2503.08390, (2025)
27. S. V. Tiablikov, Methods in the quantum theory of magnetism (Springer, 2013)
28. L. Lutsev, J. Phys. A: Math. Theor. **40**, 11791 (2007)
29. L. Lutsev, Physical Review B Condensed Matter and Materials. Physics **85**, 214413 (2012)
30. D.-L. Zhang, J. Zhu, T. Qu, D. M. Lattery, R. H. Victora, X. Wang, J.-P. Wang, Sci. Adv. 6 (2020)
31. K. Torres, A. Kuc, L. Maschio, T. Pham, K. Reidy, L. Dekanovsky, Z. Sofer, F.M. Ross, J. Klein, Adv. Funct. Mater. **33**, 2211366 (2023)
32. C.J. Morath, H.J. Maris, Phys. Rev. B **54**, 203–213 (1996)
33. R. den Teuling, R. Das, A. V. Bondarenko, E. V. Tartakovskaya, G. E. W. Bauer, Y. M. Blanter, arXiv preprint arXiv:2502.20797 (2025)
34. M.A. Tschudin, D.A. Broadway, P. Siegwolf, C. Schrader, E.J. Telford, B. Gross, J. Cox, A.E.E. Dubois, D.G. Chica, R. Rama-Eiroa, E.J.G. Santos, M. Poggio, M.E. Ziebel, C.R. Dean, X. Roy, P. Maletinsky, Nat. Commun. **15**, 6005 (2024)